

REPORT DOCUMENTATION PAGE				Form Approved OMB No. 0704-0188	
Public reporting burden for this collection of information is estimated to average 1 hour per response, including the time for reviewing instructions, searching existing data sources, gathering and maintaining the data needed, and completing and reviewing this collection of information. Send comments regarding this burden estimate or any other aspect of this collection of information, including suggestions for reducing this burden to Department of Defense, Washington Headquarters Services, Directorate for Information Operations and Reports (0704-0188), 1215 Jefferson Davis Highway, Suite 1204, Arlington, VA 22202-4302. Respondents should be aware that notwithstanding any other provision of law, no person shall be subject to any penalty for failing to comply with a collection of information if it does not display a currently valid OMB control number. PLEASE DO NOT RETURN YOUR FORM TO THE ABOVE ADDRESS.					
1. REPORT DATE (DD-MM-YYYY) 07-Mar-2011		2. REPORT TYPE Final		3. DATES COVERED (From - To) 01-Apr-2007 to 31-May-2010	
4. TITLE AND SUBTITLE Organic Photonics: Toward a New Generation of Thin Film Photovoltaics and Lasers				5a. CONTRACT NUMBER FA9550-07-1-0364	
				5b. GRANT NUMBER	
				5c. PROGRAM ELEMENT NUMBER	
6. AUTHOR(S) Forrest, Stephen R.				5d. PROJECT NUMBER	
				5e. TASK NUMBER	
				5f. WORK UNIT NUMBER	
7. PERFORMING ORGANIZATION NAME(S) AND ADDRESS(ES) Regents of the University of Michigan 1058 Wolverine Tower - DRDA Ann Arbor, MI 48109-1274				8. PERFORMING ORGANIZATION REPORT NUMBER F017357	
9. SPONSORING / MONITORING AGENCY NAME(S) AND ADDRESS(ES) USAF, AFRL DUNS 143574726 AF Office of Scientific Research 875 N. Randolph St. Room 3112 Arlington, VA 22203				10. SPONSOR/MONITOR'S ACRONYM(S) AFOSR/PKA	
				11. SPONSOR/MONITOR'S REPORT NUMBER(S) AFRL-OSR-VA-TR-2011-0023	
12. DISTRIBUTION / AVAILABILITY STATEMENT Approved for public release; distribution is unlimited.					
13. SUPPLEMENTARY NOTES					
14. ABSTRACT This program was directed at two objectives: finding a path to electrically lasing in organic semiconductors, and demonstrating very high efficiency small molecular weight solar cells. In both cases, the program was highly successful.					
15. SUBJECT TERMS Polariton lasing Nanocrystalline solar cells					
16. SECURITY CLASSIFICATION OF:			17. LIMITATION OF ABSTRACT	18. NUMBER OF PAGES 24	19a. NAME OF RESPONSIBLE PERSON Stephen R. Forrest
a. REPORT	b. ABSTRACT	c. THIS PAGE			19b. TELEPHONE NUMBER (include area code) (734) 936-2680

Organic Photonics: Toward A New Generation of Thin Film Photovoltaics and Lasers

Stephen R. Forrest

Departments of EECS, Physics and Materials Science & Engineering
University of Michigan, Ann Arbor, MI 48109 stevefor@umich.edu

I. Overview of Results

This program was directed at two objectives: finding a path to electrically lasing in organic semiconductors, and demonstrating very high efficiency small molecular weight solar cells. In both cases, the program was highly successful. The primary accomplishments can be summarized as follows (details of the two most significant results will be found after the summary:

1. Polariton lasing: Our proprietary approach is to use exciton-polaritons to result in lasing of the organic material. Here, this mixed exciton-photon state in a high Q optical microcavity is created by low intensity optical or electrical pumping. The advantage of this approach is that the emission from a single polariton state is coherent. Hence, in principle, very low pumping

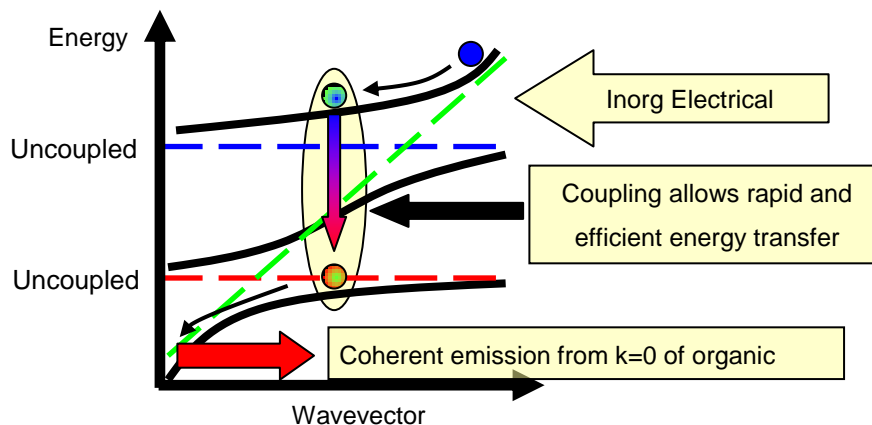


Fig. 1: Principles of polariton lasing

densities are required to obtain laser-like optical emission, making this approach ideal for electrically pumped laser applications. As shown in our previous work, direct electrical injection to create laser emission in a conventional organic OLED-type resonant cavity is unlikely to succeed. Indeed, thus far OLED emission at powers as high as $1\text{MW}/\text{cm}^2$ has failed to exhibit any trace of even the onset of lasing (e.g. line narrowing). We have concentrated our effort on creating single crystals, or near single crystals of small molecular weight organics (anthracene and tetracene) in optical microcavities. *The work has resulted in the first demonstration of a polariton laser at room temperature.* It was

based on the material, anthracene, grown in single crystal form within a high Q microcavity, and is able to function at room temperature due to the very large binding energy of organic (Frenkel) excitons. This work was published in 2010 in *Nature Photonics*. In our follow-on program, we will be attempting to electrically pump these microcavities (or an adjacent inorganic coupled cavity) to produce electrically excited lasing in organics for the first time.

2. Nanocrystalline solar cells: A key to achieving high efficiency organic solar cells is to create a high surface area bulk heterojunction, where the interconnectivity between donor and acceptor regions is nearly complete. Moreover, the ideal bulk heterojunction will consist of crystalline regions where the charge mobility is high to allow for extraction of charge. We have developed a powerful means for the growth of crystalline bulk HJs on the nanoscale using our proprietary process of organic vapor phase deposition (OVPD). Using this highly controllable process, interdigitated, crystalline structures that are on the scale of the exciton diffusion lengths in the copper phthalocyanine donor and C_{60} acceptor (~4-20 nm) have been grown. This has resulted in a three-fold improvement over the efficiency of a planar HJ cell using these same materials, achieving 4.5% power conversion efficiency (calibrated and solar spectrally corrected) for a HJ cell. The crystalline nanostructure of the cell is shown in Fig. 2. This work has been published in *Advanced Materials*. Experiments employing SnPc as the third component (absorbing in the near infrared) have proved to be quite promising. In principle, there is no limit to the number of constituent materials that can be included in a single junction cell to cover the broadest possible solar spectral range.

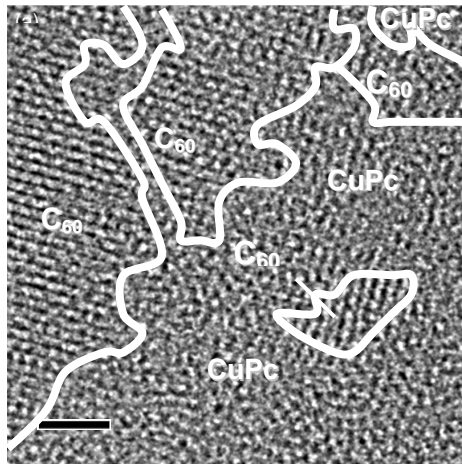


Fig. 2: Cross sectional TEM image of nanocrystalline regions of C_{60} and CuPc grown by OVPD

II. Detailed Summary of Major Accomplishments

A. Polariton Laser

The optical properties of organic semiconductors are almost exclusively described using the Frenkel exciton picture⁶. In this description, the strong Coulombic interaction between an excited electron and the charged vacancy it leaves behind (a hole) is automatically taken into account. If, in an optical microcavity, the exciton-photon interaction is strong compared to the excitonic and photonic decay rates, a second

quasiparticle, the microcavity polariton, must be introduced to properly account for this coupling⁷. Coherent, laser-like emission from polaritons has been predicted to occur when the ground-state occupancy of polaritons $\langle n_{gs} \rangle$, reaches 1 (Ref. ⁸). This process, known as polariton lasing, can occur at thresholds much lower than required for conventional lasing. Polaritons in organic semiconductors are highly stable at room temperature, but to our knowledge, there has as yet been no report of nonlinear emission from these structures. Here, we demonstrate polariton lasing at room temperature in an organic microcavity composed of a melt-grown anthracene single crystal sandwiched between two dielectric mirrors.

Polariton lasing and Bose-Einstein condensation (BEC) of polaritons have both recently been observed in inorganic semiconductors⁹⁻¹¹. However, with the exception of

the nitrides, the strong-coupling regime has only been reported at cryogenic temperatures in inorganic materials due to the small binding energy (~ 10 meV) typical of the extended Wannier-Mott excitons characteristic of these materials. In contrast, strongly-coupled organic microcavities, can readily be made to span the entire visible spectrum at room-temperature due to the high binding energy (~ 1 eV) of Frenkel excitons. In this work, we demonstrate polariton lasing in the organic semiconducting crystal anthracene, at room temperature and at a threshold below that of our best-case estimate for conventional photon lasing.

We find that upon reaching threshold, the emission shifts from a sub-linear bimolecular quenched regime, to a superlinear regime accompanied by a drastic reduction in the emission lifetime, spectral

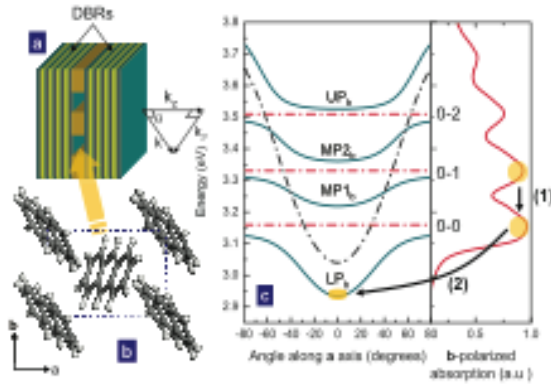


Fig. 3: Experimental structure and dispersion of the b-polarized polariton. a) Schematic showing the fabricated structure and the empty channels, prior to filling with anthracene. b) Anthracene crystal structure viewed along the [001] stacking direction. Two molecules per unit cell can be identified and the **a** and **b** crystal axes are indicated. This results in two distinct polaritons possessing an anisotropic dispersion¹⁻⁵. c) Left: Calculated dispersion of the **b**-polarized polariton along the **a**-crystal axis. The lower polariton (LP_b), middle polaritons (MP_b) and upper polariton (UP_b) branches resulting from strong coupling of the cavity photon to the intramolecular vibronics are indicated. The bare (uncoupled) dispersions of the exciton and cavity photon are also shown. Each angle can be related to the in-plane wavevector k_a . Right: Absorption spectrum of anthracene. (1) Shows fast relaxation of the photogenerated excitons to the bottom of the excitonic band (reservoir) via the emission of optical phonons. (2) Shows direct pumping of the polaritonic ground state from the exciton reservoir.

narrowing, and a thermalization of the polariton distribution function. Angle-resolved photoluminescence indicates that the microcavity remains in the strong-coupling regime above threshold, suggesting the transition from incoherent polariton emission to polariton lasing¹². Furthermore, our calculations suggest that if organic polaritonic structures approaching the thermodynamic limit¹³ can be realized, coherent emission using direct electrical injection is possible – a regime that heretofore has been inaccessible to organic materials¹⁴.

The microcavity used in this study, shown schematically in Fig. 3a, consists of a nominally 120 nm-thick crystalline anthracene film sandwiched between two, 12 period, $\text{SiN}_x/\text{SiO}_2$ distributed Bragg Reflectors (DBRs)⁴. In anthracene, two excitonic resonances are present, polarized along the **a** and **b** crystal axes. This splitting of the molecular resonance results from the Coulomb interaction between the two inequivalent molecules in the unit cell (Fig. 3b)¹⁵. Both cavity photon polarizations can couple simultaneously to these resonances and their vibronic replicas, resulting in an anisotropic dispersion possessing multiple polariton branches¹⁻⁵. The dispersion corresponding to the **b**-polarized resonance is shown in Fig. 3c.

To identify a threshold in the polariton ground state occupation, the emission spectrum at 0° was measured as a function of the pump fluence, varied using a series of metallic neutral density filters (Fig. 4). Here, the sample was pumped non-resonantly

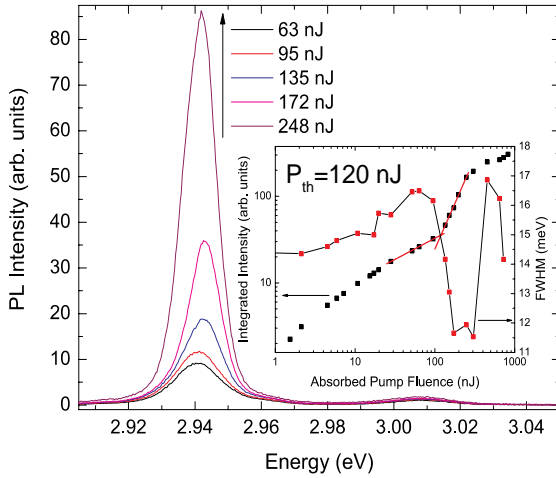


Fig. 4: **Intensity dependence.** Photoluminescence measured at $k=0$ as a function of pump fluence. Inset: Integrated area of LP_b and full width at half maximum linewidth of LP_b at $k=0$ as functions of pump fluence. The lasing threshold is defined as the intersection between the sub-linear regime dominated by bimolecular quenching, and the superlinear region.

with 150 fs, $\lambda = 360$ nm, pulses at an angle of 10° from normal incidence. The inset shows the integrated area of the **b**-polarized lower polariton (LP_b) emission peak as a function of pump fluence. This emission transitions from sub-linear at low fluence and dominated by bimolecular quenching, to superlinear above threshold ($P_{th} = 120$ nJ). Immediately below and above threshold, the intensity dependence is fit to a power law x^p with $p=0.49\pm0.02$ and $p=2.10\pm0.07$ respectively. At the highest fluences, the emission intensity saturates. On the other hand, emission from the **a**-polarized lower polariton (LP_a) remains in the sub-linear regime both

below and above threshold. We also observe a narrowing of the emission linewidth from 16.5 meV immediately below threshold to 11.5 meV above. Note that because the cavity thickness is intentionally varied over the sample area, the observed linewidth is broadened here due to spatial averaging.

A small blue shift of the polariton is observed above threshold, but this does not appear to be related to exciton-exciton interactions as in the case of inorganic semiconductors. Depending on the detuning between the excitonic resonance and the cavity mode, the polariton will blue or red-shift towards 2.94 eV. By measuring spots with different detunings, we have observed nonlinear emission from both the **a** and **b**-polarized lower polaritons (LP_a and LP_b), with the laser emission polarized accordingly. However, lasing is only observed when the detuning is such that the *polariton ground state* is located near 2.94 eV. This corresponds to the energetic separation between the exciton reservoir and the first vibronic sublevel of the *molecular ground state*. This suggests that the polariton ground state is directly populated from the reservoir.

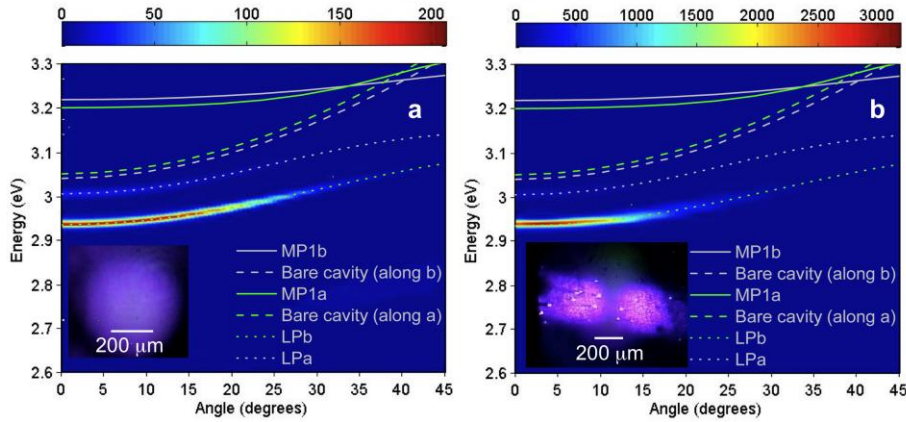


Fig. 5: **Angle resolved photoluminescence.** a) Angle-resolved photoluminescence measured below threshold. Emission from LP_a and LP_b is observed. Dashed lines corresponding to the position of the “uncoupled” cavity modes are indicated for reference. The solid line shows the position of MP1_b (not observed in PL). b) Angle-resolved photoluminescence measured above threshold. Emission is seen to still occur from the lower polariton branches and not the “uncoupled” cavity, providing strong evidence for polariton lasing. The insets show the emission spot imaged using a color CCD camera below (a) and above (b) threshold. The **b** axis is in the vertical direction.

To investigate the polariton population, angle-resolved photoluminescence was performed along the **a**-axis of the crystal with a detection cone of half angle, $\theta = 4^\circ$. Photoluminescence below threshold, at a pump fluence of $0.003P_{th}$, is shown in Fig. 5a. The observed peak positions are directly associated with the polariton dispersion, $E_{LP}(k_a, k_b=0)$, where k_a and k_b are the wavevectors along the **a** and **b** crystal axes respectively. Emission from LP_b is strongest and is TE polarized, while emission from LP_a is TM

polarized. In both cases, emission is strongest at $\theta=0^\circ$ (corresponding to zero in-plane wavevector), and decreases monotonically with increasing angle. This reflects the decreasing polariton population and increasing lifetime with increasing angle along the branch. The emission spot below threshold is shown in the inset of Fig. 5a. It is circular and Gaussian in intensity. The angle-resolved photoluminescence above threshold at a pump fluence of $1.3P_{th}$ shown in Fig. 5b, indicates that the dispersion is unchanged, confirming that the structure is still in the strong-coupling regime. However, the emission occurs almost exclusively from LP_b and becomes localized near the bottom of the branch. In addition, the emission spot changes drastically, acquiring Hermite-Gaussian TEM_{01} modal structure. In regions with a detuning where lasing does not occur, neither modal structure nor bright spots are seen at the same pump intensity. The bright emission spots observed above threshold appear to be localized near structural inhomogeneities on the film, while the two modal lobes retain the same shape on various locations on the sample where lasing occurs. Similar transverse mode profiles have resulted from anisotropy in vertical-cavity surface-emitting lasers¹⁶.

To determine the nature of the scattering mechanism responsible for populating the lower branch, we have calculated the scattering rate of a reservoir exciton to the polariton ground state via the nonradiative emission of an optical phonon¹⁷ to be $k_{nr} \sim (100\text{ns})^{-1}$ (using the molecular density $\rho=2/476.5\text{\AA}^3$, the exciton-phonon coupling constant $g \sim 1$ and the detuning $\Delta=-120$ meV). This value is large compared to the radiative lifetime of anthracene, suggesting that radiative scattering, mediated by the dipole interaction, is dominant¹⁸. We note that even below threshold, a peak in photoluminescence at an emission angle (θ) corresponding to $E_{LP}(\theta) \sim 2.94$ eV is observed⁵, highlighting the effectiveness of this scattering mechanism. This behaviour is in striking contrast to inorganic semiconductors, where relaxation occurs via multi-step relaxation along the lower branch, and where exciton-exciton interactions play a crucial role in this scattering process¹⁹.

The emission lifetime was measured with a streak camera using the same detection geometry. The time-dependence of the integrated intensity originating from LP_b is shown in Fig. 6a. At $0.018P_{th}$, the emission follows single-exponential decay at long times, with a lifetime $\tau=1.04 \pm 0.02$ ns. At higher pump fluences, the emission lifetime is further reduced at short times, along with an increase in the influence of bimolecular quenching. Above threshold, the emission decay time collapses to <30 ps and is limited by the resolution of our experimental apparatus. The short emission lifetime above threshold is a result of effective scattering from the exciton reservoir to the bottom of the lower polariton branch, and the short cavity photon lifetime compared to the nonradiative polariton decay rate.

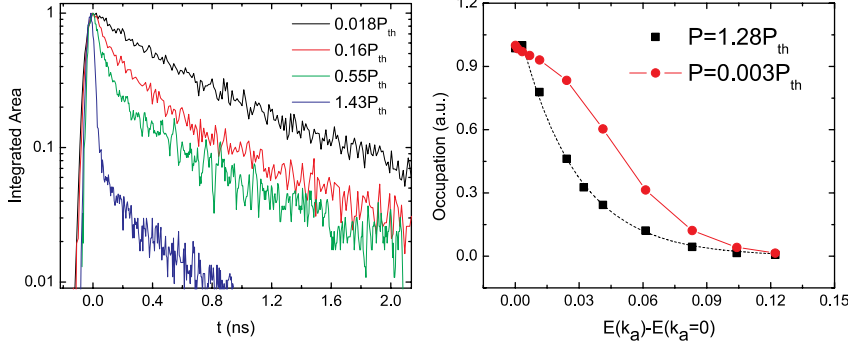


Fig. 6: **Temporal response and occupation number.** a) Photoluminescence transient taken in the normal direction ($\theta=0^\circ$ in Fig. 3a) for increasing pump fluence showing the evolution from weakly quenched, to strongly quenched, to lasing. The single-exponential decay time constant at low pump fluence (or long-times) varies between 0.7-2.5 ns, depending on the probed spot due to varying impurity and trap densities on the sample. The decay time, however, always collapses to <30 ps above threshold. b) Polariton distribution function below and above threshold. Above threshold, the distribution can be fit to a Boltzmann distribution: $n(E) \propto \exp(-\Delta E / k_b T_{lattice})$ (where $\Delta E \equiv E(k_a) - E(k_a = 0)$ and k_b is Boltzman's constant). The fit results in a lattice temperature $T_{lattice}=326K$.

the decay rate of polaritons compared to these rates. Below threshold, the system appears to be far from thermal equilibrium. Above threshold, the peak emission is found slightly off-normal at $\theta=2.5^\circ$. Indeed, this angle provides the resonance condition for direct pumping from the reservoir. However, for higher angles, the population distribution changes to a shape which is indistinguishable from a Boltzmann distribution with an activation energy corresponding to a lattice temperature $T_{lattice}=326K$. This suggests that relaxation above threshold is greatly enhanced and that even under pulsed excitation, some thermalization occurs. The population near $k=0$, however, differs from that expected for a Bose-Einstein condensate at thermal equilibrium and from Fig. 4, it is apparent that in anthracene, nonradiative decay by bimolecular annihilation severely limits the possibility of achieving extremely large ground state populations.

The observation of stimulated emission from crystalline anthracene has been reported at low temperature²⁰, but to our knowledge this is the first demonstration of lasing from crystalline anthracene. We can, nevertheless, estimate the pump density required for conventional photon lasing in the same structure. By varying the dimensions of the pump spot, we have measured a gain coefficient $\alpha \sim 20 \text{ cm}^{-1}$ at a pump density of $43 \mu\text{J}/\text{cm}^2$ ($15.9 \mu\text{J}/\text{cm}^2$ absorbed). In the microcavity, the mirror losses alone are calculated to be at least 540 cm^{-1} . Assuming the best case where the gain scales linearly with the

The lower polariton population density below and above threshold is shown in Fig. 6b. The shape of the polariton population density function is determined by the various scattering rates, and may or may not reach thermal equilibrium depending on

pump density (ignoring bimolecular quenching), we calculate a threshold $P_{th}=430 \mu\text{J}/\text{cm}^2$ for conventional lasing. At threshold for polariton lasing, however, we measure a absorbed pump density of only $P_{th}=320 \mu\text{J}/\text{cm}^2$.

Still, the distinction between polariton and photon lasing remains a subtle point in this organic semiconductor. Unlike the case of inorganic semiconductors, the Mott density is never exceeded in organic semiconductors (we know of no demonstration of a free electron-hole plasma in an organic material), and as a result, the polariton emission is never bleached. However, “transparency” is *always* exceeded for vibronic sub-levels of the ground state since these are unoccupied in thermal equilibrium. Absorption occurs from the relaxed ground state to vibronic sub-levels of the excited state, while spontaneous emission occurs from the relaxed excited state to vibronic sub-levels of the ground state. Since the peak of the amplified spontaneous emission spectrum corresponds to these transitions, gain may be contributing to the radiative scattering mechanism which populates the polariton ground state.

In inorganic microcavities, the polariton lasing threshold has been found to be as much as one order of magnitude lower than that for conventional photon lasing. However, in organic crystals with inversion symmetry (e.g. anthracene), only high order multipoles contribute to the dynamic exciton-exciton interaction which is responsible the efficient polariton-polariton scattering of inorganic semiconductors, making it relatively inefficient²¹. It is the large intramolecular phonon energy characteristic of organic materials, however, that enables direct pumping of the lower branch from the reservoir. Organic materials with efficient nonradiative scattering mechanisms such as exciton-phonon and exciton-exciton interactions may further reduce the polariton lasing threshold compared to that of conventional lasing. Indeed, we have calculated the phase diagram¹³ of the experimental structure in the thermodynamic limit (assuming an infinite particle lifetime) and find a threshold density for condensation $N_{th}= 3 \times 10^{13}/\text{cm}^3$. Direct electrical pumping of such a structure beyond threshold would be feasible with current organic light-emitting diode architectures²².

B. Nanocrystalline Organic Solar Cells

The power conversion efficiencies of organic photovoltaic (PV) cells have steadily increased since the introduction of the donor/acceptor (DA) heterojunction²³. Further improvements have been reported in entangled or “bulk-heterojunction” (BHJ) structures, where the DA interface is within an exciton diffusion length ($\sim 10\text{nm}$) of the site for photon absorption²⁴. However, the high series resistance^{25, 26} of these amorphous blends limits the active layer thickness, leading to low fill factor and reduced light absorption,

and hence a low solar energy conversion efficiency²⁷. One means to circumvent the low mobility of charge in disordered organic films has been the use of inorganic semiconductor “quantum dots”²⁸. These nanocrystals serve as charge generation sites that, when loaded into a polymer film at high density, can form a high conductivity percolating path to extract photogenerated charge from the device active region. Unfortunately, the mismatch in optical and excitonic properties between the quantum dots and the polymer matrix has limited PV cell efficiencies of photovoltaic cells based on these materials. In this work, we demonstrate that controlled crystallization of organic molecules results in a PV cell where the active layer is comprised of a nanocrystalline organic region that forms high conductivity networks for charge extraction. This cell shares many of the benefits of organic/inorganic quantum dot cells, as well as of all-organic bulk heterojunctions without many of their disadvantages. Structural analysis confirms the existence of crystalline phases of the constituent donor molecule, copper phthalocyanine (CuPc), and the acceptor, C₆₀. The new device architecture results in a three times increase of power conversion efficiency over that of an efficient planar HJ solar cell control.

To reduce cell series resistance in the organic BHJ, it is necessary to create morphological order that leads to a low resistance to charge conduction, lacking bottlenecks or islands that impede carrier extraction. Indeed, spatial ordering induced by vertical phase separation led to increase charge collection in organic/inorganic quantum dot hybrid cells from 1.7%²⁸ for a disordered cell, to 2.8%²⁹. For this reason, we recently reported organic solar cells with an ordered, interdigitated DA interface formed by crystalline donor protrusions and a planarizing acceptor layer, grown by the process of organic vapor phase deposition (OVPD). Control of organic film crystallization and morphology resulted in a low resistance, ordered, interdigitated interface that, when employed in solar cell structures, led to significantly improved efficiency over otherwise identical, planar HJs³⁰. Such an interface, however, does not increase efficiency for the materials with large exciton diffusion lengths, e.g., C₆₀, where the finite protrusion size and density do not lead to increased exciton dissociation.³¹ In the current work, we have expanded the DA crystalline interface concept into an extended bulk, highly interconnected and entangled interpenetrating network. This concept employing a thicker DA region significantly increases the HJ interface area while maintaining crystalline regions that effectively conduct charges to the opposing electrodes of the cells. This architecture opens up a range of possibilities for attaining high efficiency organic PV cells, including the mixing of three or more organic constituents in a single active region to provide full coverage of the solar spectrum.

The nanocrystalline network relies on the growth of ultrathin, alternating layers of the D and A molecules such that any given layer does not fully cover the layer that lies below. Incomplete coverage results from a combination of lack of surface wetting, and control of film morphology and crystalline texture using OVPD.

The growth of nanocrystalline DA networks was simulated by including gas phase molecular transport, surface diffusion, and re-evaporation back into gas phase,³² with results shown in Fig. 7a. Periodic boundary conditions apply in both in-plane directions. Organic molecules randomly originate far from the substrate in the gas phase, and diffuse toward the substrate. Upon reaching a solid surface, the admolecule diffuses on the solid film surface, where the jumping rate between two sites, i and j , is determined by the site energy E_i and E_j as:³²

$$K_{i \rightarrow j} = \nu f(E_i, E_j). \quad (1)$$

Here ν is the lattice vibration factor and:

$$f(E_i, E_j) = \begin{cases} \exp\left(-\frac{E_j - E_i}{k_B T}\right) & \text{if } E_j > E_i \\ 1 & \text{if } E_j < E_i \end{cases}. \quad (2)$$

The site energy, E_i , is the sum of van der Waals interactions between the admolecule and all proximal neighboring molecules. The interaction energy between nearest neighbors are taken as 0.867 eV (CuPc – CuPc),³³ 1.5 eV (C₆₀ – C₆₀),^{34, 35} and 0.044 eV (CuPc – C₆₀),³⁶ respectively. Since the interaction between like molecules is much larger than the interaction between unlike molecular pairs, similar molecules tend to aggregate. The simulated growth of the network begins on a continuous layer of copper phthalocyanine (CuPc) on a transparent conductive substrate, e.g., indium-tin-oxide (ITO). Then a thin layer of C₆₀ is deposited on top of the underlying, continuous CuPc layer. The aggregates in the C₆₀ layer do not provide a full coverage of the underlayer, leaving part of the CuPc exposed. A second, thin CuPc layer is then deposited, partially covering the C₆₀ layer with portions of the second CuPc layer directly contacting the first, continuous CuPc layer. By continuously alternating the deposition of C₆₀ and CuPc, 3D interpenetrating nanocrystalline networks of C₆₀ and CuPc are formed. The growth simulation indicates a monotonic increase of the interface area as the number of alternating DA bilayers is increased. As shown in Fig. 7a, the final interface area in a nanocrystalline cell with 6 C₆₀/CuPc pairs is 11 times that of a planar interface. The root mean square (rms) surface roughness of the nanocrystalline films also increases, and reaches a maximum of approximately 4 nm. The final step is the growth of a continuous C₆₀ layer on top of the network, planarizing the film surface to prevent shorts³⁰.

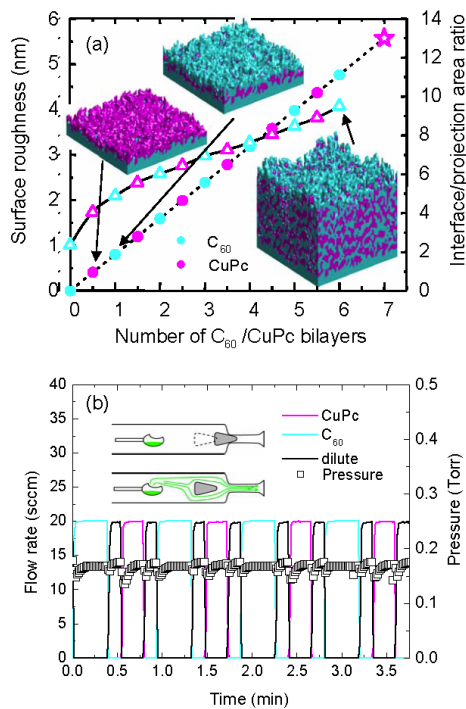


Fig. 7: Simulation and growth methods of $[C_{60}(3\text{nm}) / \text{CuPc}(3\text{nm})]_n$ nanocrystalline donor/acceptor (DA) networks. **a**, Simulation of the growth progression of a six period network. The plot shows, the root mean square (rms) surface roughness (open triangles) and the interface area relative to a planar DA junction (filled circles) as functions of number of bilayers. The star shows the final area ratio after the 6-period network is covered by a continuous C_{60} planarizing layer. The three inset pictures show the evolution of the film structure and surface morphology of the C_{60} (magenta) / CuPc (cyan) nanocrystals at different growth stages in the progression, as well as the CuPc network formed after the sixth C_{60} /CuPc cycle, where 3-D interconnected networks can be clearly seen. **b**, Mass flow rates and pressure change recorded during the organic vapor phase deposition of the C_{60} /CuPc structure. Top inset: Barrel valve in the off position, preventing organics from diffusing out of the barrel. Bottom inset: Carrier gas conveying organic molecules out of the barrel when the valve is in the on position.

We used OVPD to grow the crystalline network PV cells. Large nitrogen gas flow rates (150 sccm for CuPc and 100 for C_{60}) and low substrate temperatures ($T_{\text{sub}} = 4 \pm 1$ °C) were used for the bottom and top continuous layers, resulting in a flat surface. Smaller nitrogen flow rates (20 sccm for both CuPc and C_{60}) and higher T_{sub} (15 ± 1 °C) were used to promote crystallization during the discontinuous layer growth.³⁷ The crystalline film texture of an OVPD-grown multilayer (grown by the process illustrated in Fig. 7b) is confirmed by transmission electron microscopy (TEM), x-ray diffraction (XRD) and atomic force microscopy (AFM), as shown in Fig. 8. A cross-sectional TEM image of $[\text{CuPc}(6.1\text{nm})/C_{60}(6.1\text{nm})]_{10}$ is shown in Fig. 8a. (Here, the notation $[D(x\text{ nm})/A(y\text{ nm})]_n$ refers to the thicknesses x , y of the D and A layers, respectively, and n is the number of DA pairs.) The CuPc and C_{60} phases are similar to those observed in a crystalline bilayer film³⁸. The C_{60} phase has clearly ordered, close packed molecular planes, while the monoclinic CuPc lattice appears less ordered since the image is not taken along the projection of a single, crystallographic plane.³⁹ Both electron and x-ray diffraction confirm the existence of crystalline domains of CuPc and C_{60} . Crystalline domain sizes range from 5 nm to 10 nm, similar to those found in homogeneous films of C_{60} , but smaller than ZnPc crystals obtained by thermal evaporation^{40, 41}. We obtained similar TEM images of $[\text{CuPc}(3.1\text{ nm})/C_{60}(3.1\text{ nm})]_{17}$, where the crystallites are similar in shape but have slightly smaller sizes, as expected. High-angle annular dark-field images confirm the presence

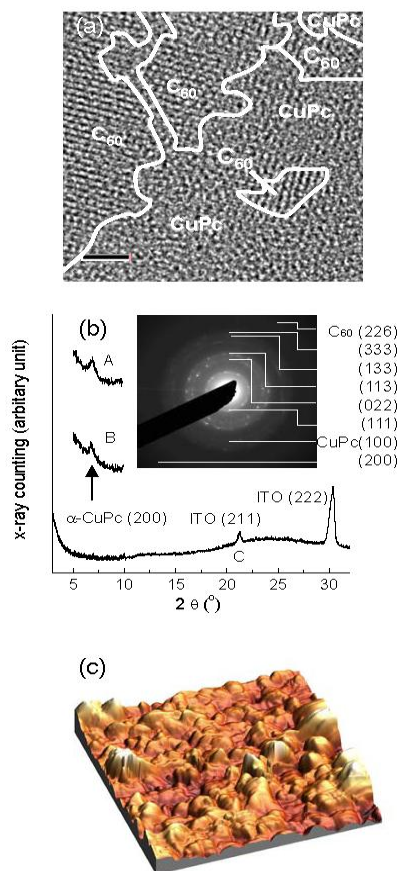


Fig. 8: Structural characterization of a C_{60} /CuPc nanocrystalline film grown on an indium-tin-oxide (ITO) substrate. **a**, Cross sectional high-resolution TEM image of a $[CuPc(6.1nm)/C_{60}(6.1nm)]_{10}$ film, showing nanocrystalline domains indicated by white curves that locate the domain boundaries. Scale bar=5 nm. **b**, X-ray diffraction pattern of an OVPD grown A. $[C_{60}(3.5\text{ nm})/CuPc(3.5\text{ nm})]_5$ film, and B. a $[C_{60}(1.9\text{ nm})/CuPc(1.9\text{ nm})]_{10}$ film. C. A 100-nm thick C_{60} :CuPc = 1:1 mixed film grown by vacuum thermal co-evaporation. The CuPc (200) and ITO (211), (222) indices are indicated. Inset: Plan-view selective area diffraction pattern taken for the film in **a**. The diffraction indices of α -CuPc and C_{60} are marked. Well defined diffraction spots indicate crystalline order. **c**, Atomic force microscopic surface morphology of the same film in **a**, showing an rms roughness of 12.7 nm in the $100 \times 100\text{ nm}^2$ area.

of CuPc aggregates, with sizes comparable to the domain sizes observed in Fig. 8a.

A selected area electron diffraction image of the same $[CuPc(6.1nm)/C_{60}(6.1nm)]_{10}$ film in plan-view (Fig. 8b, inset) shows diffraction spots corresponding to ordered domains of α -CuPc⁴² and face centered cubic (fcc) C_{60} ⁴³. The crystallites have a similar size and distribution as those seen in cross-sectional view. The well defined diffraction spots indicate a high degree of crystalline order and orientation within the region of the probe beam. In addition, the XRD patterns of $[CuPc(3.5nm)/C_{60}(3.5nm)]_5$ and $[CuPc(1.9nm)/C_{60}(1.9nm)]_{10}$ shown in Fig. 8b, confirm the existence of α -CuPc in the two samples. No C_{60} diffraction peaks can be identified in the scanning range due to its large lattice constant ($a = 14.16\text{ \AA}$)⁴³. These structural studies show that crystalline phases are obtained by alternating the growth of the D and A materials using OVPD, as opposed to amorphous CuPc: C_{60} mixed films grown by co-evaporation²⁶ (bottom scan, Fig. 8b), where the crystalline phase separation is limited^{44,26, 27,40, 41}. As shown in Fig. 2c, the surface morphology of the same $[CuPc(6.1nm)/C_{60}(6.1nm)]_{10}$ film observed by AFM shows the crystalline texture with an rms roughness of 12.7 nm, reflecting the roughing effect (c.f. Fig. 7a) caused by the crystallite growth over the ITO substrate whose rms roughness < 3 nm.

The absorption spectra of the nanocrystalline films are fit to the linear sum of the neat CuPc and C_{60} absorption spectra

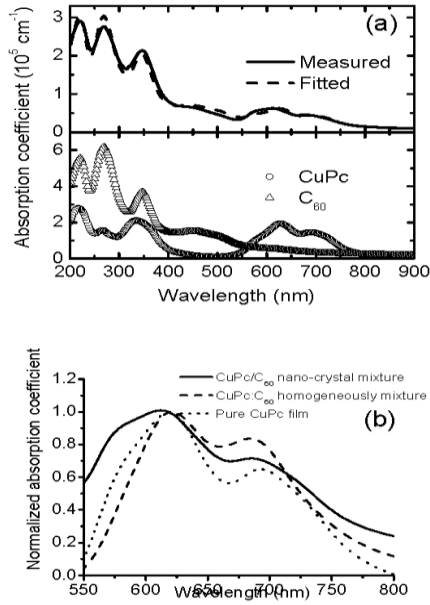


Fig. 9: Absorption coefficients (α) of CuPc and C_{60} films on fused silica substrates. a. Absorption of a nanocrystalline $[C_{60}(3.1 \text{ nm})/CuPc(3.1 \text{ nm})]_{17}$ film, and a fit by $\alpha_{NC} = 0.48\alpha_{C60} + 0.23\alpha_{CuPc}$. The absorption of the pure films are shown in the lower part of the figure. **b.** Normalized absorption spectra in the low-energy *O*-band of CuPc.

(α_{CuPc} and α_{C60} , respectively). Figure 9a shows the absorption coefficient of $[CuPc(3.1 \text{ nm})/C_{60}(3.1 \text{ nm})]_{17}$ grown on a fused quartz substrate, fit using $\alpha_{NC} = 0.48\alpha_{C60} + 0.23\alpha_{CuPc}$. Films with different DA cycle thicknesses are fit using similar expressions. Pure CuPc films have two peaks centered at wavelengths of $\lambda=620$ and 695 nm , corresponding to dimer and monomer absorption, respectively⁴². For amorphous CuPc: C_{60} mixtures, the absorption at $\lambda=695 \text{ nm}$ is enhanced due to an increased intermolecular distance^{26, 44, 45}. By comparison, the nanocrystalline layer peak at $\lambda=695 \text{ nm}$ is less pronounced than in the mixed film, implying the presence of a high density of CuPc crystallites (Fig. 9b)⁴⁴. The asymmetry in the CuPc and C_{60} absorption obtained in our fits may be an effect of differing crystal sizes for these two molecular constituents.

We note that these crystalline structures are in a stable, rather than metastable structure, as observed in annealed mixtures of CuPc and 3, 4, 9, 10- perylenetetracarboxylic bis-benzimidazole

(PTCBI)⁴⁶. Furthermore, compared to phase-separated polymer cells prepared by annealing at $110\text{-}150 \text{ }^{\circ}\text{C}$,^{25, 37} the small molecular weight films in our PV cells have high glass transition temperatures ($> 400 \text{ }^{\circ}\text{C}$). Further phase separation of these cells is, therefore, not expected to occur under normal operating conditions and required operational lifetimes (10-20 years) of such devices.

A series of $CuPc(14.5 \pm 0.2 \text{ nm})/[C_{60}(3.2 \pm 0.2 \text{ nm})/CuPc(3.2 \pm 0.2 \text{ nm})]_n/C_{60}(40.0 \pm 0.5 \text{ nm}) / BCP(10 \text{ nm})/Ag$ (BCP=bathocuproine) double heterojunction PV cells⁴⁷ were fabricated, where n ranged from 0 to 12. Here, BCP was used as an exciton blocking layer. The nominal thicknesses of the $C_{60}(3.2 \text{ nm})/CuPc(3.2 \text{ nm})$ multilayers were varied between 6.4 and 76.8 nm, keeping $C_{60}:CuPc = 1$ for all samples. Hence, for $n = 12$, the total organic active film thickness was $t=141 \text{ nm}$, which exceeds $t=100 \text{ nm}$, typical of that of a conventional, bilayer small molecular weight cell. This, in turn, increases the optical absorption due to its exponential dependence on thickness (i.e., cell responsivity follows $(1 - \exp[-\alpha t])$), where α is the absorption coefficient of the organic

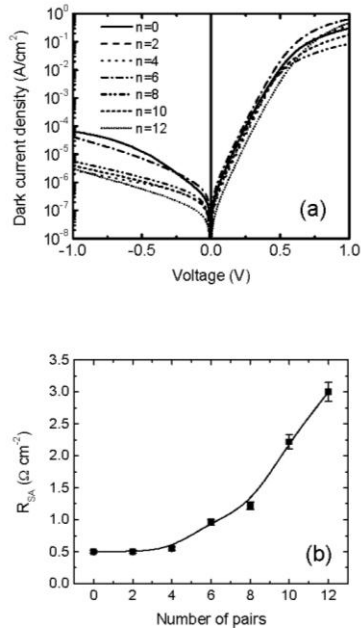


Fig. 10: The performance of CuPc(14.5±0.2nm) / [C₆₀(3.2±0.2nm) / CuPc(3.2±0.2nm)]_n / C₆₀(50.0±0.5nm) / BCP (10nm) / Ag solar cells, with n varying from 0 to 12, and the total thickness of the active layers varying from 54.5 to 141 nm. a. Dark current density - applied voltage (J - V) characteristics b. Specific resistance (R_{sa}) as a function of n and C₆₀/CuPc nanocrystalline layer thickness, calculated by fitting the dark J - V characteristics using the ideal diode equation.

material. Furthermore, the top C₆₀ layer is thicker than used in the optimized bilayer device^{47, 48}, as necessary to planarize the rough film surface³⁰ (c.f. Fig. 8c).

The dark current density-voltage (J - V) characteristics of all cells have rectification ratios $> 10^4$ at ± 1 V, as shown in Fig. 10a. Fitting the forward J - V curves using the ideal diode equation^{30, 48} yields the specific series resistance, R_{SA} , as a function of the number of alternating DA pairs (and hence total active layer thickness) in Fig. 10b. The bilayer ($n = 0$) cell has $R_{SA} = 0.5 \Omega \cdot \text{cm}^2$, gradually increasing to $3.0 \Omega \cdot \text{cm}^2$ for $n = 12$. That R_{SA} increases by a factor of ~ 6 for a cell only twice as thick indicates that the nanocrystalline region is not completely free of bottlenecks to charge conduction. However, multilayers with fewer periods show only a 2 to 3 times increase in R_{SA} , suggesting that disorder increases significantly only for the deepest stacks.

The photoresponse of the same cells as in Fig. 11 measured under simulated $100 \pm 4 \text{ mW/cm}^2$ AM 1.5G solar irradiation are shown in Fig. 11a. The short circuit current (J_{SC}), open circuit voltage (V_{OC}) and fill factor (FF) are plotted in Fig. 11b. With n increasing from 2 to 6, J_{SC} significantly increases by nearly a factor of 3, from $5.6 \pm 0.1 \text{ mA/cm}^2$ in the bilayer cell to $17.0 \pm 0.2 \text{ mA/cm}^2$, and then drops as n

is increased further, due to the high series resistance of the thickest cells with large and entangled crystalline networks. In the same figure, V_{OC} increases from 0.44 ± 0.01 V in the bilayer cell ($n = 0$), and gradually increasing to 0.50 ± 0.01 V at $n = 12$. Finally, FF decreases slightly from 0.57 ± 0.01 at $n = 0$ to 0.56 at $n = 6$, and drops to 0.44 ± 0.01 at $n = 12$, once more reflecting the increase of resistance in the deepest stacks, as shown in Fig. 10b.

The external quantum efficiency (EQE) as a function of wavelength⁴⁹ is shown in Fig. 11c. The EQE peak, centered between $\lambda = 430$ and 470 nm, results from C₆₀ absorption⁵⁰, whereas the peaks at $\lambda = 620$ and 695 nm are due to CuPc absorption²⁶ (c.f. Fig. 3a). As the number of C₆₀/CuPc pairs increases from $n = 0$ to $n = 6$, the EQE

increases rapidly, i.e., the $\lambda=620$ nm peak increases from 25% to 76%, and the peak at $\lambda=450$ nm increases from 22% to 64%, both showing a 3-fold increase with n . In fact, in a previously reported photodetector composed of *continuous* ultrathin (≥ 0.5 nm) CuPc/PTCBI multilayer stacks grown in vacuum, an EQE of up to 75% was achieved at a reverse bias of -10 V.⁵¹ In contrast to that device, the nanocrystalline solar cell with its entangled heterointerface shows the same large EQE at zero bias, implying success in achieving continuous conductive pathways. The EQE decreases at larger n due to a lower carrier collection efficiency resulting from increased resistance, possibly indicating that the percolating conducting paths formed by the network of nanocrystallites are interrupted by bottlenecks or islands. Note that the broad peak corresponding to C_{60} absorption shifts to shorter wavelength as n increases, as a result of the optical field changes with the thickness.

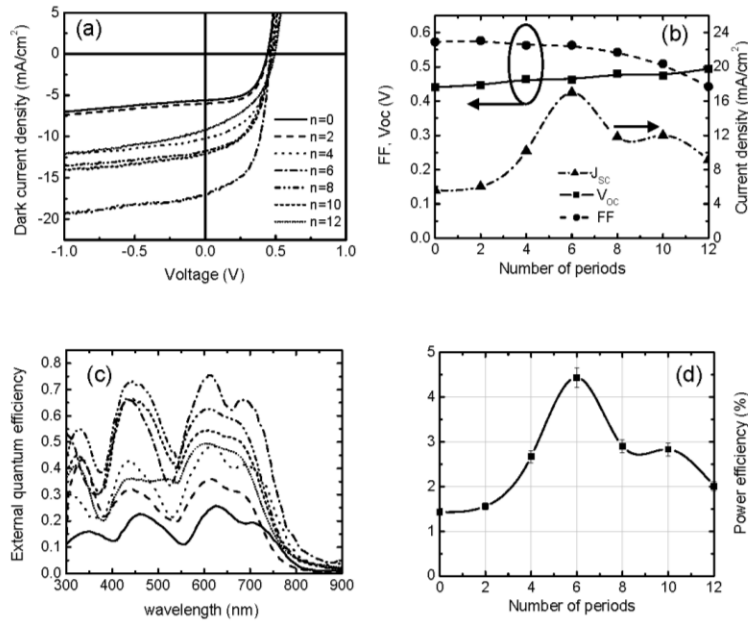


Fig. 11: Parameters affecting room-temperature power-conversion efficiency of the solar cells in Fig. 4. a. J - V characteristics at simulated AM 1.5 global 105 ± 5 mW/cm² solar illumination. **b.** Short circuit current density (J_{sc}), open circuit voltage (V_{oc}) and fill factor (FF) as functions of the number of C_{60} /CuPc growth cycles, n . **c.** External quantum efficiency (η_{EQE}) spectra of devices with different n . **d.** Power conversion efficiency (η_p) as a function of n and C_{60} /CuPc nanocrystalline layer thickness.

Previously, it was shown that the growth of an organized interdigitated DA interface results in a 2.7 times increase in efficiency in a CuPc/PTCBI solar cell³⁰ over its planar analog, but that architecture showed no improvement when the CuPc/ C_{60} system was used³¹. This lack of improvement was attributed to the long (~ 40 nm) exciton diffusion length²⁴ in C_{60} , which exceeded the interdigitated feature width. The CuPc/PTCBI cell characteristic diffusion lengths were < 10 nm, or half of the

feature size, hence leading to the efficiency improvement observed. In contrast, the photoresponse of CuPc and C_{60} in the nanocrystalline cells both increase by more than 3

times, suggesting that the high carrier mobility in the extended, percolating networks is primarily responsible for their improvement in efficiency.

The power conversion efficiency, η_p , is plotted as a function of n in Fig. 11d. The photocurrent and power efficiencies of unpackaged devices were measured in air referenced to an NREL-calibrated Si detector. Here, $\eta_p = 1.4 \pm 0.1\%$ in the bilayer device ($n=0$) increases by a factor of 3, to a maximum of $4.4 \pm 0.2\%$ at $n = 6$, corresponding to a total thickness of the nanocrystalline region of 38nm, which is almost double the optimum thickness of a mixed CuPc:C₆₀ solar cell active region²⁷. The efficiency rolls off to $2.1 \pm 0.1\%$ at $n = 12$. The power efficiency of the unoptimized CuPc/C₆₀ bilayer control cell is consistent with that reported by other groups,^{52, 53} although it is not as high as the best reported for planar cells using the same materials system grown by vacuum thermal evaporation⁴⁸. The solar cell efficiency showed minor (~5 %) degradation when exposed to ambient for 24 hours.

By controlling the organic molecule crystallization conditions, we used OVPD to deposit an organic solar cell architecture incorporating an all-organic nanocrystalline network which has both a large DA HJ interface area favorable for exciton dissociation, and a large thickness for light absorption.⁵⁴ The crystalline order introduces only a small series resistance with increasing thickness, and our demonstration has resulted in a three-fold increase of efficiency over planar HJ controls in a one-to-one comparison. The solar cell active region thicknesses are >100nm, eliminating shorts commonly observed in thinner cells, while also increasing the active region thickness, leading to an exponential increase in light absorption. Furthermore, changing the nanocrystalline size^{30, 31}, varying the DA ratio⁴⁴, incorporating more than two molecular components to obtain broader coverage of the solar spectrum, and employing multiple cells in a tandem structure⁴⁰ may lead to even higher efficiencies. We emphasize that the devices reported here do not represent a practical demonstration, which would only be possible with large solar cell modules with long operational lifetimes. Rather, our work demonstrates that control of the fully organic nanostructure morphology leads to highly interconnected nanocrystalline networks that significantly improve both exciton dissociation and charge collection that have potential application to a new generation of solar energy conversion devices.

III. Publications Under AFOSR Sponsorship

1. "Strong exciton-photon coupling in organic materials" R. J. Holmes and S. R. Forrest, invited, *Organic Electron.*, **8**, 77 (2007).

2. "Offset energies at organic semiconductor heterojunctions and their influence on the open-circuit voltage of thin-film solar cells", B. P. Rand, D. P. Burk and S. R. Forrest, *Phys. Rev. B*, **75**, 115327 (2007).
3. "Real-time Monitoring of Organic Vapor-Phase Deposition of Molecular Thin Films Using High-Pressure Reflection High-Energy Electron Diffraction ", R. Lunt, J. B. Benziger and S. R. Forrest, *Appl. Phys. Lett.*, **90**, 181932 (2007).
4. "Enhancement-Mode Buried Channel $\text{In}_{0.7}\text{Ga}_{0.3}\text{As}/\text{In}_{0.52}\text{Al}_{0.48}\text{As}$ MOSFET with High-k Gate Dielectrics", Y. Sun, E. W. Kiewra, S. J. Koester, N. Ruiz, A. Callegari, K. E. Fogel, D. K. Sadana, J. Fompeyrine, D. J. Webb, J.-P. Locquet, M. Sousa, R. Germann, K. T. Shiu and S. R. Forrest, *IEEE Electron Dev. Lett.*, **28**, 473 (2007).
5. "Organic Electronics and Optoelectronics", S. R. Forrest and M. E. Thompson, *Chem. Rev.*, **107**, 923 (2007).
6. "Near-infrared sensitive small molecule organic photovoltaic cells based on chloroaluminum phthalocyanine", R. F. Bailey-Salzman, B. P. Rand, and S. R. Forrest, *Appl. Phys. Lett.*, **91**, 013508 (2007).
7. "The limits to accumulation of electric field-stabilized geminate polaron-pairs in an organic semiconductor thin film", N.C. Giebink, S.R. Forrest, *Phys. Rev. B*, **76**, 075318 (2007).
8. "Growth of an ordered crystalline organic heterojunction", R. R. Lunt, J. B. Benziger and S. R. Forrest, *Adv. Mater.*, **19**, 4229 (2007).
9. "Efficient solar cells using all-organic nanocrystalline networks", F. Yang, K. Sun, and S. R. Forrest, *Adv. Mater.*, **19**, 4166 (2007).
10. "Giant Davydov splitting of the lower polariton branch in a polycrystalline tetracene microcavity", S. Kena-Cohen, S. R. Forrest, *20th Ann. Meet. IEEE-LEOS Proc.*, **1**, 125 (2007)
11. "Simultaneous heterojunction organic solar cells with broad spectral sensitivity", F. Yang, R. R. Lunt and S. R. Forrest, *Appl. Phys. Lett.*, **92**, 053310 (2008).
12. "Giant Davydov splitting of the lower polariton branch in a polycrystalline tetracene microcavity" S. Kena-Cohen and S. R. Forrest, *Phys. Rev. B*, **77**, 073205 (2008).
13. "Intrinsic luminance loss in phosphorescent small-molecule organic light emitting devices due to bimolecular annihilation reactions". N.C. Giebink, B.W. D'Andrade, M.S. Weaver, P.B. Mackenzie, J.J. Brown, M.E. Thompson, and S.R. Forrest, *J. Appl. Phys.*, **103**, 044509 (2008).
14. "Photocurrent generation in nanostructured organic solar cells", F. Yang and S. R. Forrest, *ACS Nano*, **2**, 1022 (2008).
15. "Strong exciton-photon coupling in an organic single crystal microcavity", S. Kéna-Cohen, M. Davanço and S.R. Forrest, *Phys. Rev. Lett.*, **101**, 116401 (2008).

16. “Resonant Rayleigh scattering from an anisotropic organic single crystal microcavity”, S. Kéna-Cohen, M. Davanço and S.R. Forrest, *Phys. Rev. B*, **78**, 153102 (2008).
17. “Organic photovoltaics using tetraphenylbenzoporphyrin complexes as donor layers”, M. D. Perez, C. Borek, P. I. Djurovich, E. I. Mayo, R. R. Lunt, S. R. Forrest and M. E. Thompson, *Adv. Mater.*, **21**, 1517 (2009).
18. “Open circuit voltage enhancement due to reduced dark current in small molecule photovoltaic cells”, N. Li, B. E. Lassiter, R. R. Lunt, G. Wei, and S. R. Forrest, *Appl. Phys. Lett.*, **94**, 023307 (2009).
19. “Exciton Diffusion Lengths of Organic Semiconductor Thin Films Measured by Spectrally Resolved Photoluminescence Quenching”, R. R. Lunt, N. C. Giebink, A. A. Belak, J.B. Benziger, and S. R. Forrest, *J. Appl. Phys.*, **105**, 053711 (2009).
20. “Measurement of the Mean Inner Potentials of Anthracene and Naphthalene”, R. R. Lunt, S. Kéna-Cohen, J. B. Benziger, and S. R. Forrest, *Phys. Rev. Lett.*, **102**, 065504 (2009).
21. “Temporal Response of Optically Pumped Organic Semiconductor Lasers and its Implication for Reaching Threshold Under Electrical Excitation,” N. C. Giebink and S. R. Forrest, *Phys. Rev. B*, **79**, 073302 (2009).
22. “Enhanced open circuit voltages in subphthalocyanine/C₆₀ organic photovoltaic cells”, K. L. Mutolo, E. I. Mayo, B. P. Rand, S. R. Forrest and M. E. Thompson, *J. Am. Chem. Soc.*, **128**, 8108 (2009).
23. “Tilted Bulk Heterojunction Organic Photovoltaic Cells Grown by Oblique Angle Deposition”, N. Li and S. R. Forrest, *Appl. Phys. Lett.*, **95**, 123309 (2009).
24. “Relationship between Crystalline Order and Exciton Diffusion Length in Molecular Organic Semiconductors”, R. R. Lunt, J. B. Benziger, and S. R. Forrest, *Adv. Mater.*, **22**, 1233 (2010).
25. “Room-temperature polariton lasing in an organic single crystal microcavity”, S. Kéna-Cohen and S. R. Forrest, *Nature Photon.*, **4**, 371 (2010).

IV. Students Supported

1. Fan Yang, PhD, 2008, current employment: Qualcomm
2. Rhonda Bailey-Salzmann, MSE, 2008
3. Noel C. Giebink, PhD, 2009, current employment: Argonne National Lab
4. Stephane Kéna-Cohen, PhD, 2010, current employment: Imperial College, London
5. Richard R. Lunt, III, PhD, 2010, current employment: Michigan State U.

V. New Discoveries/Inventions/Patent Disclosures

1. "Apparatus and Method for Deposition for Organic Thin Films," Univ. Michigan Disclosure 3787, U.S. Patent filing date 2/13/2008, Patent application no. 12/030,362. Inventors: Fan Yang and S.R. Forrest.
2. "Growth of Ordered Crystalline Organic Films," Univ. Michigan Disclosure 3796, U.S. Patent filing date 8/22/2008, Patent application no. 12/197,195. Inventors: S.R. Forrest and R. Lunt.
3. "Enhanced External Quantum Efficiency in Organic Solar Cells," Univ. Michigan Disclosure 3797, U.S. Patent filing date 7/9/2008, Patent application no. 61/079,401. Inventors: Noel C. Giebink and S.R. Forrest.
4. "Multi-Component Organic Solar Cells and Photodetectors with Broad Spectrum Response," Univ. Michigan Disclosure 3888, U.S. Patent filing date 11/2/2007, Patent application no. 60/984,966. Inventors: S.R. Forrest and Fan Yang.
5. "Simultaneous Heterojunction Organic Solar Cells with Broad Spectral Sensitivity," Univ. Michigan Disclosure 3956, U.S. Patent filing date 1/8/2008, Patent application no. 61/019,730. Inventors: S.R. Forrest, R. Lunt and Fan Yang.
6. "Use of Organic Semiconductor-Semiconducting Carbon Nanotube Heterojunctions in photovoltaic and Photoelectric Devices," Univ. Michigan Disclosure 3968, U.S. Patent filing date 5/1/2008, Patent application no. 61/049,594.
7. "Inverted Organic Photosensitive Devices," Univ. Michigan Disclosure 4090, U.S. Patent filing date 10/26/2009, Patent application no. 12/605,958. Inventors: S.R. Forrest and Rhonda F. Bailey-Salzman.
8. "Organic Tandem Solar Cells," Univ. Michigan Disclosure 4113, U.S. Patent filing date 9/25/2009, Patent application no. 12/567,633. Inventors: S.R. Forrest, Brian E. Lassiter and Guodan Wei.
9. "Tandem Organic Solar Cells Incorporating CuPc and SubPc and Donor Materials," Univ. Michigan Disclosure 4243, U.S. Patent filing date 11/28/2008, Patent application no. 61/118,529. Inventors: S.R. Forrest, Brian E. Lassiter and Guodan Wei.
10. "Enhancement of Organic Photovoltaic Cell Open Circuit Voltage Using Electron/Hole Blocking Exciton Blocking Layers," Univ. Michigan Disclosure 4261, U.S. Patent filing date 1/12/2010, Patent application no. 12/686,305. Inventors: S.R. Forrest and Ning Li.
11. "Focusing Luminescent and Thermal Radiation Concentrators," Univ. Michigan Disclosure 4301, dated 2/11/2009. Inventors: S.R. Forrest and Noel C. Giebink.
12. "Organic Laser," Univ. Michigan Disclosure 4311, U.S. Patent filing date 7/29/2009, Patent application no. 12/511,797. Inventors: S.R. Forrest, Noel C. Giebink and Stephane Kena-Cohen.

13. "Apparatus and Method for Deposition of Organic Thin Films," Univ. Michigan Disclosure 4332, U.S. Patent filing date 5/18/2009, Patent application no. 12/467,468. Inventors: S.R. Forrest, R. Lunt and Fan Yang.
14. "Light Trapping Architecture for Photovoltaic and Photodetector Applications," Univ. Michigan Disclosure 4340, dated 3/5/2009. Inventors: R. Lunt, Michael Sloatsky and S.R. Forrest.
15. "Bulk Heterojunction Organic Photovoltaic Cells Made by Glancing Angle Deposition," Univ. Michigan Disclosure 4441, U.S. Patent filing date 7/27/2010, Patent application no. 12/843,949. Inventors: S.R. Forrest and Ning Li.
16. "High Efficiency Inverted Organic Photovoltaic Devices," Univ. Michigan Disclosure 4540, U.S. Patent filing date 10/9/2009, Patent application no. 61/250,379. Inventors: S.R. Forrest, Brian E. Lassiter and Xiaoran Tong.
17. "Thermal and Solvent Annealing Influence on the Performance of Solution-Processed Squaraine/C60 Planar and Squaraine/PC70BM Bulk Heterojunction Photovoltaic Cells," Univ. Michigan Disclosure 4677, U.S. Patent filing date 4/8/2010, Patent application no. 61/322,039. Inventors: S.R. Forrest and Guodan Wei.
18. "Method of Improving Exciton Dissociation at Organic Donor-Acceptor Heterojunctions," Univ. Michigan Disclosure 4696, U.S. Patent filing date 5/5/2010, Patent application no. 61/331,798. Inventors: S.R. Forrest and Noel C. Giebink.

References

1. H. Zoubi and G. C. La Rocca, Phys. Rev. B **71** (23), 235316 (2005).
2. M. Litinskaya, P. Reineker and V. M. Agranovich, Phys. Status Solidi A **201** (4), 646-654 (2004).
3. S. Kena-Cohen and S. R. Forrest, Phys. Rev. B **77** (7), 073205 (2008).
4. S. Kena-Cohen, M. Davanço and S. R. Forrest, Phys. Rev. Lett. **101** (11), 116401 (2008).
5. S. Kena-Cohen, M. Davanco and S. R. Forrest, Phys. Rev. B **78** (15), 153102 (2008).
6. M. Pope, C. E. Swenberg and M. Pope, *Electronic processes in organic crystals and polymers*, 2nd ed. (Oxford University Press, New York, 1999).
7. D. G. Lidzey, D. D. C. Bradley, M. S. Skolnick, T. Virgili, S. Walker and D. M. Whittaker, Nature (London) **395** (6697), 53-55 (1998).
8. A. Imamoglu, R. J. Ram, S. Pau and Y. Yamamoto, Phys. Rev. A **53** (6), 4250-4253 (1996).
9. J. Kasprzak, M. Richard, S. Kundermann, A. Baas, P. Jeambrun, J. M. J. Keeling, F. M. Marchetti, M. H. Szymanska, R. Andre, J. L. Staehli, V. Savona, P. B.

- Littlewood, B. Deveaud and L. S. Dang, *Nature (London)* **443** (7110), 409-414 (2006).
10. H. Deng, G. Weihs, D. Snoke, J. Bloch and Y. Yamamoto, *Proc. Natl. Acad. Sci. U. S. A.* **100** (26), 15318-15323 (2003).
 11. S. Christopoulos, G. B. H. von Hagersthal, A. J. D. Grundy, P. G. Lagoudakis, A. V. Kavokin, J. J. Baumberg, G. Christmann, R. Butte, E. Feltin, J. F. Carlin and N. Grandjean, *Phys. Rev. Lett.* **98** (12), 126405 (2007).
 12. G. Malpuech, A. Kavokin and F. P. Laussy, *Phys. Status Solidi A* **195** (3), 568-578 (2003).
 13. G. Malpuech, Y. G. Rubo, F. P. Laussy, P. Bigenwald and A. V. Kavokin, *Semicond. Sci. Technol.* **18** (10), S395-S404 (2003).
 14. N. C. Giebink and S. R. Forrest, *Phys. Rev. B* **79** (7), 073302-073306 (2009).
 15. A. S. Davydov, *Theory of molecular excitons*. (Plenum Press, New York., 1971).
 16. P. Debernardi, G. P. Bava, C. Degen, I. Fischer and W. Elsasser, *IEEE J. Quantum. Electron.* **38** (1), 73-84 (2002).
 17. M. Litinskaya, P. Reineker and V. M. Agranovich, *J. Lumin.* **110** (4), 364-372 (2004).
 18. L. Mazza, L. Fontanesi and G. C. La Rocca, *Phys. Rev. B* **80** (23), 235314 (2009).
 19. F. Tassone and Y. Yamamoto, *Phys. Rev. B* **59** (16), 10830-10842 (1999).
 20. O. S. Avanesyan, V. A. Bendersky, V. K. Brikenshtein, V. L. Broude, A. G. Lavrushko, I. I. Tartakovsky and P. G. Filippov, *Quantum Electron.* **7** (4), 403 (1977).
 21. M. Litinskaya, *Phys. Rev. B* **77** (15), 155325 (2008).
 22. J. R. Tischler, M. S. Bradley, V. Bulovic, J. H. Song and A. Nurmikko, *Phys. Rev. Lett.* **95** (3), 036401 (2005).
 23. C. W. Tang, *Appl. Phys. Lett.* **48** (2), 183-185 (1986).
 24. P. Peumans, A. Yakimov and S. R. Forrest, *J. Appl. Phys.* **93** (7), 3693-3723 (2003).
 25. W. Ma, C. Yang, X. Gong, K. Lee and A. J. Heeger, *Adv. Funct. Mater.* **15** (10), 1617-1622 (2005).
 26. B. P. Rand, J. Xue, S. Uchida and S. R. Forrest, *J. Appl. Phys.* **98**, 124902 (2005).
 27. J. Xue, B. P. Rand, S. Uchida and S. R. Forrest, *Adv. Mater.* **17** (1), 66-71 (2005).
 28. W. U. Huynh, J. J. Dittmer and A. P. Alivisatos, *Science* **295**, 2425 (2002).
 29. B. Sun, H. J. Snaith, A. S. Dhoot, S. Westenhoff and N. C. Greenham, *J. Appl. Phys.* **97**, 014914 (2004).
 30. F. Yang, M. Shtein and S. R. Forrest, *Nat. Mater.* **4** (1), 37-41 (2005).

31. F. Yang, M. Shtein and S. R. Forrest, J. Appl. Phys. **98** (1), 014906-014901 (2005).
32. R.-F. Xiao, J. I. D. Alexander and F. Rosenberger, Phys. Rev. A **43** (6), 2977 (1991).
33. D.-J. Liu, R. L. B. Selinger and J. D. Weeks, The Journal of Chemical Physics **105** (11), 4751-4760 (1996).
34. V. P. Antropov, O. Gunnarsson and O. Jepsen, Phys. Rev. B **46** (20), 13647 (1992).
35. R. W. Lof, M. A. van Veenendaal, B. Koopmans, H. T. Jonkman and G. A. Sawatzky, Phys. Rev. Lett. **68** (26), 3924 (1992).
36. M. Fendrich, T. Wagner, M. Stohr and R. Moller, Physical Review B (Condensed Matter and Materials Physics) **73** (11), 115433-115437 (2006).
37. G. Li, V. Shrotriya, J. Huang, Y. Yao, T. Moriarty, K. Emery and Y. Yang, Nature Materials **4** (11), 864–868 (2005).
38. V. Bhosle, J. T. Prater, F. Yang, D. Burk, S. R. Forrest and J. Narayan, J. Appl. Phys. **in press** (2007).
39. J. R. FRYER, J. Electr. Micro. Tech. **11**, 310-325 (1989).
40. B. Maennig, J. Drechsel, D. Gebeyehu, P. Simon, F. Kozlowski, A. Werner, F. Li, S. Grundmann, S. Sonntag, M. Koch, K. Leo, M. Pfeiffer, H. Hoppe, D. Meissner, N. S. Sariciftci, I. Riedel, V. Dyakonov and J. Parisi, Appl. Phys. A **79** (1), 1-14 (2004).
41. P. Simon, B. Maennig and H. Lichte, Adv. Funct. Mater. **14** (7), 669-676 (2004).
42. C. C. Leznoff and A. B. P. Lever, *Phthalocyanines : properties and applications*. (VCH, New York, NY, 1989).
43. P. A. Heiney, J. E. Fischer, A. R. McGhie, W. J. Romanow, A. M. Denenstein, J. P. M. Jr., A. B. Smith and D. E. Cox, Phys. Rev. Lett. **66** (22), 2911-2914 (1991).
44. P. Sullivan, S. Heutz, S. M. Schultes and T. S. Jones, Appl. Phys. Lett. **84** (7), 1210-1212 (2004).
45. S. Heutz, P. Sullivan, B. M. Sanderson, S. M. Schultes and T. S. Jones, Sol. Energ. Mat. Sol. Cells **83** (2-3), 229-245 (2004).
46. P. Peumans, S. Uchida and S. R. Forrest, Nature **425**, 158-162 (2003).
47. P. Peumans and S. R. Forrest, Appl. Phys. Lett. **79** (1), 126-128 (2001).
48. J. Xue, S. Uchida, B. P. Rand and S. Forrest, Appl. Phys. Lett. **84** (16), 3013-3015 (2004).
49. (American Society for Testing and Materials, 2001), Vol. Standard ASTM E1021 – 95, pp. 1-5.

- 50. S. Mochizuki, M. Sasaki and R. Ruppin, J. Phys.: Condens. Matter **10** (10), 2347 (1998).
- 51. P. Peumans, V. Bulovic and S. R. Forrest, Appl. Phys. Lett. **76** (26), 3855-3857 (2000).
- 52. K. Fostiropoulos, M. Vogel, B. Mertesacker and A. Weidinger, Proceedings of the SPIE - The International Society for Optical Engineering **4801**, 1-6 (2003).
- 53. Z. R. Hong, C. J. Liang, X. Y. Sun and X. T. Zeng, J. Appl. Phys. **100** (9), 93711 (2006).
- 54. Z. R. Hong, B. Maennig, R. Lessmann, M. Pfeiffer, K. Leo and P. Simon, Appl. Phys. Lett. **90** (20), 203505-203503 (2007).